Journal of Computational Physics 228 (2009) 5040–5056

Contents lists available at ScienceDirect

Journal of Computational Physics

journal homepage: www.elsevier.com/locate/jcp

Divergence-free reconstruction of magnetic fields and WENO schemes for magnetohydrodynamics

Dinshaw S. Balsara *

Department of Physics, University of Notre Dame, Notre Dame, IN 46556, United States

ARTICLE INFO

Article history:
Received 15 October 2008
Received in revised form 17 March 2009
Accepted 30 March 2009
Available online 7 April 2009

Keywords:
Magnetohydrodynamics
Numerical methods
Reconstruction
WENO schemes

ABSTRACT

In a pair of earlier papers the author showed the importance of divergence-free reconstruction in adaptive mesh refinement problems for magnetohydrodynamics (MHD) and the importance of the same for designing robust second order schemes for MHD. Second order accurate divergence-free schemes for MHD have shown themselves to be very useful in several areas of science and engineering. However, certain computational MHD problems would be much benefited if the schemes had third and higher orders of accuracy. In this paper we show that the reconstruction of divergence-free vector fields can be carried out with better than second order accuracy. As a result, we design divergence-free weighted essentially non-oscillatory (WENO) schemes for MHD that have order of accuracy better than second. A multi-stage Runge–Kutta time integration is used to ensure that the temporal accuracy matches the spatial accuracy. While this is achieved quite simply up to third order in time, going beyond third order is most simply achieved by using the ADER-WENO schemes that are detailed in a companion paper. (ADER stands for Arbitrary Derivative Riemann Problem.) Accuracy analysis is carried out and it is shown that the schemes meet their design accuracy for smooth problems. Stringent tests are also presented showing that the schemes perform well on those tests.

1. Introduction

The magnetohydrodynamic (MHD) equations play an important role in many areas of astrophysics, space physics and engineering. Typical applications in those areas require one to capture flow on a range of scales in a way that is as dissipation-free as possible. As a result, there has been considerable interest in bringing accurate and reliable numerical methods to bear on this problem. The MHD system of equations can be written as a set of hyperbolic conservation laws. As a result, early efforts concentrated on straightforwardly applying second order total variation diminishing (TVD) techniques to the MHD equations. This was done by Brio and Wu [13], Zachary et al. [41], Powell [33], Dai and Woodward [16], Ryu and Jones [35], Roe and Balsara [34], Balsara [1,2], Falle et al. [25], Dedner et al. [18] and Crockett et al. [15]. The schemes by Powell [33] and Dedner et al. [18] were based on modifying the MHD equations to arrive at innovative methods for transporting away any divergence that might be generated in the magnetic field. Recent efforts have focused on understanding the structure of the induction equation:

$$\frac{\partial \mathbf{B}}{\partial t} + \nabla \times (c\mathbf{E}) = 0 \tag{1}$$

* Tel.: +1 574 631 9639; fax: +1 574 631 5952.
E-mail address: dbalsara@nd.edu

0021-9991/$ - see front matter © 2009 Elsevier Inc. All rights reserved.
doi:10.1016/j.jcp.2009.03.038

and the divergence-free evolution that it implies for the magnetic field. In Eq. (1), **B** is the magnetic field, **E** is the electric field and c is the speed of light. The magnetic field starts out divergence-free because of the absence of magnetic monopoles and Eq. (1) ensures that it remains divergence-free for all time. The electric field is given by:

$$c\mathbf{E} = -\mathbf{v} \times \mathbf{B} \tag{2}$$

where **v** is the fluid velocity. For the rest of this paper we will simplify the notation by making the transcription $c\mathbf{E} \rightarrow \mathbf{E}$. We pick CGS units because they are commonly used in astrophysics. The methods presented here go through just as easily in any other units. Brackbill and Barnes [11] have shown that violating the $\nabla \cdot \mathbf{B} = 0$ constraint leads to unphysical plasma transport orthogonal to the magnetic field. This comes about because violating the constraint results in the addition of extra source terms in the momentum and energy equations. Yee [40] was the first to formulate divergence-free schemes for electromagnetism. Brecht et al. [12] and DeVore [20] did the same for flux corrected transport (FCT)-based MHD. Evans and Hawley [24] presented a divergence-free scheme for MHD that was based on an artificial viscosity formulation. Following Brecht et al. [12], Evans and Hawley [24] realized that the divergence-free constraint had to be respected, inventing the term constrained transport to describe such schemes. Dai and Woodward [17], Ryu et al. [36], Balsara and Spicer [9,10], Balsara [4], Toth [39], Londrillo and DelZanna [32], Gardiner and Stone [26] and Li [31] showed that simple extensions of higher order Godunov schemes permit one to formulate divergence-free time-update strategies for the magnetic field. Balsara and Kim [6] intercompared divergence-cleaning and divergence-free schemes for numerical MHD. They found that if the test problems are made stringent enough the schemes that are based on divergence-cleaning show significant inadequacies when used for astrophysical applications. Thus it is advantageous to design robust schemes for numerical MHD that are divergence-free, as was done in [4]. In that paper we used the divergence-free reconstruction of vector fields from Balsara [3] to present a formulation that overcame several inconsistencies in previous formulations.

Higher order schemes for MHD have been attempted. Jiang and Wu [30] and Balsara and Shu [8] experimented with weighted essentially non-oscillatory (WENO) schemes. Another line of effort stems from the work of Londrillo and DelZanna [32]. These schemes were based on a finite difference formulation. For certain types of applications, especially those involving non-uniform meshes or adaptive solution strategies, finite volume formulations become essential. We therefore present a finite volume, divergence-free scheme for MHD that goes beyond second order of accuracy. We rely on efficient WENO interpolation strategies that were designed in Balsara et al. [7] to make a high order reconstruction. The novel element introduced in this paper consists of extending the divergence-free reconstruction of magnetic fields from Balsara [3,4] to all orders up to fourth. When coupled with an appropriately accurate Runge–Kutta (RK) time integration scheme by Shu and Osher [37,38], we get a set of WENO schemes that have a spatial and temporal accuracy that exceeds that of second order schemes.

In Balsara et al. [5] we presented a new class of higher order schemes for the Euler equations. In such formulations the lower moments of the solution are retained while the higher moments are reconstructed, resulting in low storage schemes with better than second order accuracy. Balsara et al. [7] extended some of the interpolation techniques from Balsara et al. [5] to present high accuracy schemes for the Euler and MHD equations. Building on their work in Dumbser et al. [21], we also presented extremely efficient ADER (for Arbitrary Derivative Riemann Problem) schemes for second to fourth order accurate temporal evolution of the Euler and MHD equations. Furthermore, we presented efficient strategies for constructing the high order accurate, space–time averaged fluxes and electric fields that are needed in a high accuracy MHD scheme. Since the divergence-free reconstruction of magnetic fields at high orders is a challenging problem in its own right, a thorough exposition of that problem was deferred to the present paper. As a result, Balsara et al. [7] and the present paper complement each other. A reader seeking to make the most efficient implementation of a finite volume scheme for divergence-free MHD should couple the divergence-free reconstruction presented here with the ADER-WENO techniques. The computational cost of the resulting schemes are catalogued in the companion paper on ADER-WENO schemes, where it is shown that the increasing cost with increasing accuracy is handily offset by an improvement in the quality of the solution provided by the scheme. The divergence-free reconstruction presented here can also be used with Runge–Kutta time-stepping to obtain adequate schemes for divergence-free MHD. Such schemes prove easier to code up and are presented here. However, our experience has been that once one goes past second order the RK-WENO schemes are not as computationally efficient as ADER-WENO schemes, and the reasons for this observation have already been catalogued in [21]. To obtain fourth or higher order of accuracy in space and time, we in fact recommend use of the ADER-WENO schemes instead of the RK-WENO schemes proposed here.

In Section 2 we catalogue the divergence-free reconstruction of vector fields for higher order schemes. In Section 3 we provide a step by step description of the scheme. In Section 4 we provide an accuracy analysis and in Section 5 we present several test problems.

2. Higher order divergence-free reconstruction of vector fields

Most finite volume schemes that are designed to evolve the magnetic field in divergence-free fashion try to obtain a discrete form of the divergence-free constraint over finite volumes which coincide with the definition of the fluid variables. The only exceptions are a pair of schemes presented in Toth [39] where the discrete form of the divergence-free constraint is asserted on a mesh that is dual to the mesh on which the fluid variables are defined. For most applications, especially when adaptive solution strategies are desired, it is most advantageous to have a scheme where the divergence-free constraint and

the fluid variables are defined on the same set of finite volumes. For all such schemes, it is essential to define the components of the magnetic fields at the face-centers and we follow that trend here.

In this section we study the divergence-free reconstruction of a face-centered divergenceless vector field for schemes with better than second order accuracy. In particular, we focus on the third and fourth order cases because they can be listed succinctly and are likely to be generally useful. The second order accurate divergence-free reconstruction of vector fields was studied for Cartesian meshes in Balsara [3]. In [4] we extended this to logically rectangular meshes with diagonal metrics. In that paper we also considered the second order accurate divergence-free reconstruction of vector fields on tetrahedral meshes and that too can be extended to higher orders. Since the method was described in detail in [3], in this paper we will focus on cataloguing results for the higher order case. The reader who wants a detailed description is referred to the above-mentioned papers.

For the rest of this work we assume that each zone has been mapped to a unit cube with local coordinates $(x,y,z) \in [-1/2,1/2]\times[-1/2,1/2]\times[-1/2,1/2]$. A natural set of modal basis functions within that zone or on its faces would consist of tensor products of the Legendre polynomials $P_0(x)$, $P_1(x)$ and $P_2(x)$. The first few Legendre polynomials are given by:

$$P_0(x)=1;\quad P_1(x)=x;\quad P_2(x)=x^2-\frac{1}{12};\quad P_3(x)=x^3-\frac{3}{20}x;\quad P_4(x)=x^4-\frac{3}{14}x^2+\frac{3}{560} \tag{3}$$

The above Legendre polynomials have just been suitably scaled to the local coordinates of the zone being considered. The x-component of the magnetic field in the upper and lower x-faces of this zone can be projected into these bases as:

$$\begin{aligned} B_x(x=\pm 1/2,y,z) = {} & B_0^{x\pm} + B_y^{x\pm}P_1(y) + B_z^{x\pm}P_1(z) && \leftarrow \text{ second order}\\ & + B_{yy}^{x\pm}P_2(y) + B_{yz}^{x\pm}P_1(y)P_1(z) + B_{zz}^{x\pm}P_2(z) && \leftarrow \text{ third order}\\ & + B_{yyy}^{x\pm}P_3(y) + B_{yyz}^{x\pm}P_2(y)P_1(z) + B_{yzz}^{x\pm}P_1(y)P_2(z) + B_{zzz}^{x\pm}P_3(z) && \leftarrow \text{ fourth order} \end{aligned} \tag{4}$$

Here $B_0^{x\pm}$, $B_y^{x\pm}$ and $B_z^{x\pm}$ are the moments that would be needed in a second order accurate representation in the basis functions that we have chosen. $B_{yy}^{x\pm}$, $B_{zz}^{x\pm}$ and $B_{yz}^{x\pm}$ are the additional moments for a third order accurate representation in the same set of basis functions. $B_{yyy}^{x\pm}$, $B_{yyz}^{x\pm}$, $B_{yzz}^{x\pm}$ and $B_{zzz}^{x\pm}$ are the further moments that are needed for a fourth order accurate representation, again in the same set of basis functions. Consequently, while Eq. (4) shows all the facial moments that are needed up to fourth order, the arrows in Eq. (4) show the terms that are needed for each specific order of accuracy. We can write similar expressions for the y- and z-components of the field in the appropriate zone faces as:

$$\begin{aligned} B_y(x,y=\pm 1/2,z) = {} & B_0^{y\pm} + B_x^{y\pm}P_1(x) + B_z^{y\pm}P_1(z) && \leftarrow \text{ second order}\\ & + B_{xx}^{y\pm}P_2(x) + B_{xz}^{y\pm}P_1(x)P_1(z) + B_{zz}^{y\pm}P_2(z) && \leftarrow \text{ third order}\\ & + B_{xxx}^{y\pm}P_3(x) + B_{xxz}^{y\pm}P_2(x)P_1(z) + B_{xzz}^{y\pm}P_1(x)P_2(z) + B_{zzz}^{y\pm}P_3(z) && \leftarrow \text{ fourth order} \end{aligned} \tag{5}$$

$$\begin{aligned} B_z(x,y,z=\pm 1/2) = {} & B_0^{z\pm} + B_x^{z\pm}P_1(x) + B_y^{z\pm}P_1(z) && \leftarrow \text{second order}\\ & + B_{xx}^{z\pm}P_2(x) + B_{xy}^{z\pm}P_1(x)P_1(y) + B_{yy}^{z\pm}P_2(y) && \leftarrow \text{ third order}\\ & + B_{xxx}^{z\pm}P_3(x) + B_{xxy}^{z\pm}P_2(x)P_1(y) + B_{xyy}^{z\pm}P_1(x)P_2(y) + B_{yyy}^{z\pm}P_3(y) && \leftarrow \text{ fourth order} \end{aligned} \tag{6}$$

To reconstruct the field in the interior of the zone we pick the following functional forms for the fields:

$$\begin{aligned} B_x(x,y,z) = {} & a_0 + a_xP_1(x) + a_yP_1(y) + a_zP_1(z)\\ & + a_{xx}P_2(x) + a_{xy}P_1(x)P_1(y) + a_{xz}P_1(x)P_1(z) && \leftarrow \text{ second order}\\ & + a_{yy}P_2(y) + a_{xyy}P_1(x)P_2(y) + a_{zz}P_2(z) + a_{xzz}P_1(x)P_2(z) + a_{yz}P_1(y)P_1(z) + a_{xyz}P_1(x)P_1(y)P_1(z)\\ & + a_{xxx}P_3(x) + a_{xxy}P_2(x)P_1(y) + a_{xxz}P_2(x)P_1(z) && \leftarrow \text{ third order}\\ & + a_{yyy}P_3(y) + a_{xyyy}P_1(x)P_3(y) + a_{yyz}P_2(y)P_1(z) + a_{xyyz}P_1(x)P_2(y)P_1(z)\\ & + a_{yzz}P_1(y)P_2(z) + a_{xyzz}P_1(x)P_1(y)P_2(z) + a_{zzz}P_3(z) + a_{xzzz}P_1(x)P_3(z)\\ & + a_{xxxx}P_4(x) + a_{xxxy}P_3(x)P_1(y) + a_{xxxz}P_3(x)P_1(z)\\ & + a_{xxyy}P_2(x)P_2(y) + a_{xxzz}P_2(x)P_2(z) && \leftarrow \text{ fourth order} \end{aligned} \tag{7}$$

$$\begin{aligned} B_y(x,y,z) = {} & b_0 + b_xP_1(x) + b_yP_1(y) + b_zP_1(z)\\ & + b_{yy}P_2(y) + b_{xy}P_1(x)P_1(y) + b_{yz}P_1(y)P_1(z) && \leftarrow \text{ second order}\\ & + b_{xx}P_2(x) + b_{xxy}P_2(x)P_1(y) + b_{zz}P_2(z) + b_{yzz}P_1(y)P_2(z) + b_{xz}P_1(x)P_1(z) + b_{xyz}P_1(x)P_1(y)P_1(z)\\ & + b_{yyy}P_3(y) + b_{xyy}P_1(x)P_2(y) + b_{yyz}P_2(y)P_1(z) && \leftarrow \text{ third order}\\ & + b_{xxx}P_3(x) + b_{xxxy}P_3(x)P_1(y) + b_{xxz}P_2(x)P_1(z) + b_{xxyz}P_2(x)P_1(y)P_1(z)\\ & + b_{xzz}P_1(x)P_2(z) + b_{xyzz}P_1(x)P_1(y)P_2(z) + b_{zzz}P_3(z) + b_{yzzz}P_1(y)P_3(z)\\ & + b_{yyyy}P_4(y) + b_{xyyy}P_1(x)P_3(y) + b_{yyyz}P_3(y)P_1(z)\\ & + b_{xxyy}P_2(x)P_2(y) + b_{yyzz}P_2(y)P_2(z) && \leftarrow \text{ fourth order} \end{aligned} \tag{8}$$

$$
\begin{aligned}
B_z(x,y,z) = {} & c_0 + c_x P_1(x) + c_y P_1(y) + c_z P_1(z) \\
& + c_{zz} P_2(z) + c_{xz} P_1(x) P_1(z) + c_{yz} P_1(y) P_1(z) \qquad \leftarrow \text{ second order} \\
& + c_{xx} P_2(x) + c_{xxz} P_2(x) P_1(z) + c_{yy} P_2(y) + c_{yyz} P_2(y) P_1(z) + c_{xy} P_1(x) P_1(y) + c_{xyz} P_1(x) P_1(y) P_1(z) \\
& + c_{zzz} P_3(z) + c_{xzz} P_1(x) P_2(z) + c_{yzz} P_1(y) P_2(z) \qquad \leftarrow \text{ third order} \\
& + c_{xxx} P_3(x) + c_{xxxz} P_3(x) P_1(z) + c_{xxy} P_2(x) P_1(y) + c_{xxyz} P_2(x) P_1(y) P_1(z) \\
& + c_{xyy} P_1(x) P_2(y) + c_{xyyz} P_1(x) P_2(y) P_1(z) + c_{yyy} P_3(y) + c_{yyyz} P_3(y) P_1(z) \\
& + c_{zzzz} P_4(z) + c_{xzzz} P_1(x) P_3(z) + c_{yzzz} P_1(y) P_3(z) \\
& + c_{xxzz} P_2(x) P_2(z) + c_{yyzz} P_2(y) P_2(z) \qquad \leftarrow \text{ fourth order}
\end{aligned} \tag{9}
$$

The rationale for picking this set of moments follows from Balsara [3]. Relative to the format followed in [3], a slight rearrangement of the functional forms has been made in the previous three equations to cast them in terms of the basis functions. Analogous to Eq. (4), Eq. (7) shows the terms that have to be included to achieve second, third and fourth order accuracy. Eqs. (8) and (9) have a structure that is similar to Eq. (7) and the corresponding terms that are needed with increasing accuracy are easily identified. The procedure for enforcing the divergence-free constraint is entirely similar to the one in [3]. It consists of applying the differential form of the divergence-free condition $\nabla \cdot \mathbf{B} = 0$ to all the polynomials in Eqs. (7)–(9) and setting the terms at each order to zero. While Balsara [3] illustrates this procedure in detail for second order, some details for the third and fourth order cases have been provided in Appendix A.

We now provide the formulae for obtaining the coefficients in Eq. (7) using the coefficients in Eqs. (4)–(6). To obtain the coefficients in Eq. (8) make the cyclic rotation of variables, $a \to b$, b $\to c$, c $\to a$, x $\to y$, y $\to z$ and $z \to x$, in the formulae below. Similarly, to obtain the coefficients in Eq. (9) make the cyclic rotation of variables, $a \to c$, b $\to a$, c $\to b$, x $\to z$, y $\to x$ and $z \to y$. Note that the formulae in this section should be implemented in code in the same sequence as described here.

The description of the fourth order divergence-free reconstruction starts with this paragraph. Matching the modal basis functions with cubic terms at the $x = \pm 1/2$ boundaries gives:

$$
\begin{aligned}
a_{yyy} &= \frac{1}{2}\left(B^{x+}_{yyy} + B^{x-}_{yyy}\right); \quad a_{xyyy} = B^{x+}_{yyy} - B^{x-}_{yyy} \\
a_{yyz} &= \frac{1}{2}\left(B^{x+}_{yyz} + B^{x-}_{yyz}\right); \quad a_{xyyz} = B^{x+}_{yyz} - B^{x-}_{yyz} \\
a_{yzz} &= \frac{1}{2}\left(B^{x+}_{yzz} + B^{x-}_{yzz}\right); \quad a_{xyzz} = B^{x+}_{yzz} - B^{x-}_{yzz} \\
a_{zzz} &= \frac{1}{2}\left(B^{x+}_{zzz} + B^{x-}_{zzz}\right); \quad a_{xzzz} = B^{x+}_{zzz} - B^{x-}_{zzz}
\end{aligned} \tag{10}
$$

Eq. (10) gives us the coefficients a_{yyy}, a_{xyyy}, a_{yyz}, a_{xyyz}, a_{yzz}, a_{xyzz}, a_{zzz} and a_{xzzz} in Eq. (7). Making the analogous match of the cubic terms at the $y = \pm 1/2$ boundaries in Eq. (8) give us b_{zzz}, b_{yzzz}, b_{xzz}, b_{xyzz}, b_{xxz}, b_{xxyz}, b_{xxx} and b_{xxxy}. It is worth pointing out that making a cyclic rotation of the variables in Eq. (10) also yields the same coefficients that are needed in Eq. (8). Matching the cubic terms at the $z = \pm 1/2$ boundaries for Eq. (9) gives us c_{xxx}, c_{xxxz}, c_{xxy}, c_{xxyz}, c_{xyy}, c_{xyyz}, c_{yyy} and c_{yyyz}. Notice too that making another cyclic rotation of variables also yields the coefficients for Eq. (9). We now apply the divergence-free constraint to the quartic terms in Eqs. (7)–(9). After making an SVD minimization of the integral of the reconstructed magnetic energy over the zone w.r.t. the coefficients a_{xxxy}, a_{xxxz}, a_{xxyy} and a_{xxzz} (see Appendix A), the resulting constraints are:

$$
a_{xxxx} = -\frac{1}{4}(b_{xxxy} + c_{xxxz}); \quad a_{xxxy} = -\frac{7}{30} c_{xxyz}; \quad a_{xxxz} = -\frac{7}{30} b_{xxyz}; \quad a_{xxyy} = -\frac{3}{20} c_{xyyz}; \quad a_{xxzz} = -\frac{3}{20} b_{xyzz} \tag{11}
$$

Notice that the right hand sides of Eq. (11) are available by this point in the computation so that Eq. (11) can be used to obtain the coefficients a_{xxxx}, a_{xxxy}, a_{xxxz}, a_{xxyy} and a_{xxzz} in Eq. (7). A cyclic rotation of variables gives us the constraints for the coefficients in Eq. (8) and yields b_{yyyy}, b_{yyyz}, b_{xyyy}, b_{yyzz} and b_{xxyy}. Likewise a cyclic rotation of variables gives us the coefficients in Eq. (9) and yields c_{zzzz}, c_{xzzz}, c_{yzzz}, c_{xxzz} and c_{yyzz}. All the terms that are evaluated in this paragraph will be needed in the subsequent formulae when fourth order reconstruction is carried out. However, for reconstruction at third and second orders they can all be set to zero.

The description of the third order divergence-free reconstruction starts with this paragraph. This paragraph also continues our description of the fourth order reconstruction. Matching the modal basis functions with quadratic terms at the $x = \pm 1/2$ boundaries gives:

$$
\begin{aligned}
a_{yy} &= \frac{1}{2}\left(B^{x+}_{yy} + B^{x-}_{yy}\right) - \frac{1}{6} a_{xxyy}; \quad a_{xyy} = B^{x+}_{yy} - B^{x-}_{yy} \\
a_{yz} &= \frac{1}{2}\left(B^{x+}_{yz} + B^{x-}_{yz}\right); \quad a_{xyz} = B^{x+}_{yz} - B^{x-}_{yz} \\
a_{zz} &= \frac{1}{2}\left(B^{x+}_{zz} + B^{x-}_{zz}\right) - \frac{1}{6} a_{xxzz}; \quad a_{xzz} = B^{x+}_{zz} - B^{x-}_{zz}
\end{aligned} \tag{12}
$$

Eq. (12) provides a_{yy}, a_{xyy}, a_{yz}, a_{xyz}, a_{zz} and a_{xzz} all of which are needed in Eq. (7). Making a cyclic rotation of variables in Eq. (12) yields the analogous terms in Eq. (8), i.e. b_{zz}, b_{yzz}, b_{xz}, b_{xyz}, b_{xx} and b_{xxy}, all of which are needed in Eq. (8). Likewise, another

cyclic rotation of variables gives the coefficients c_{xx}, c_{xxz}, c_{xy}, c_{xyz}, c_{yy} and c_{yyz} that are needed in Eq. (9). We are now ready to apply the constraints on the cubic terms in Eqs. (7)–(9). After making an SVD minimization of the integral of the reconstructed magnetic energy over the zone w.r.t. the coefficients a_{xxy} and a_{xxz} (see Appendix A) we get:

$$a_{xxx} = -\frac{1}{3}(b_{xxy} + c_{xxz}); \quad a_{xxy} = -c_{xyz}/4; \quad a_{xxz} = -b_{xyz}/4 \tag{13}$$

Eq. (13) gives us the coefficients a_{xxx}, a_{xxy} and a_{xxz}in Eq. (7). Analogous terms in Eqs. (8) and (9) can now be made via a cyclic rotation of variables so that we obtain b_{yyy}, b_{yyz}, b_{xyy}, c_{zzz}, c_{xzz} and c_{yzz}. This paragraph again gives us all the terms that will be needed in the subsequent formulae when third or fourth order reconstruction is carried out. However, for second order divergence-free reconstruction the coefficients that have been obtained in this and the previous paragraph are set to zero.

Our description of the second order divergence-free reconstruction starts with this paragraph. The present paragraph also continues our description of the third or fourth order reconstruction. Matching the modal basis functions with linear terms at the $x = \pm 1/2$ boundaries gives:

$$\begin{aligned} a_y &= \frac{1}{2}\left(B_y^{x+} + B_y^{x-}\right) - \frac{1}{6}a_{xxy}; \quad a_{xy} = \left(B_y^{x+} - B_y^{x-}\right) - \frac{1}{10}a_{xxxy} \\ a_z &= \frac{1}{2}\left(B_z^{x+} + B_z^{x-}\right) - \frac{1}{6}a_{xxz}; \quad a_{xz} = \left(B_z^{x+} - B_z^{x-}\right) - \frac{1}{10}a_{xxxz} \end{aligned} \tag{14}$$

Eq. (14) provides the coefficients a_y, a_{xy}, a_z and a_{xz} that are needed in Eq. (7). Analogous terms in Eqs. (8) and (9) can now be made via a cyclic rotation of variables. Thus one cyclic rotation of variables applied to Eq. (14) provides us b_z, b_{yz}, b_x and b_{xy}. Another such rotation of variables yields c_x, c_{xz}, c_y and c_{yz}. The constraint applied to the quadratic terms in Eqs. (7)–(9) gives:

$$a_{xx} = -\frac{1}{2}(b_{xy} + c_{xz}) - \frac{3}{35}a_{xxxx} - \frac{1}{20}(b_{xyyy} + c_{xzzz}) \tag{15}$$

Analogous terms in Eqs. (8) and (9) can now be made by applying cyclic rotations to variables in Eq. (15) and those rotations yield b_{yy} and c_{zz}.

Matching the constant terms at the $x = \pm 1/2$ boundaries gives:

$$a_0 = \frac{1}{2}\left(B_0^{x+} + B_0^{x-}\right) - \frac{1}{6}a_{xx} - \frac{1}{70}a_{xxxx}; \quad a_x = \left(B_0^{x+} - B_0^{x-}\right) - \frac{1}{10}a_{xxx} \tag{16}$$

Eq. (1) provides the coefficients a_0 and a_x that are needed in Eq. (7). Analogous terms in Eqs. (8) and (9) can now be made to get b_0, b_y, c_0 and c_z. The constraint applied to the linear terms in Eqs. (7)–(9) gives:

$$(a_x + b_y + c_z) + \frac{1}{10}(a_{xxx} + b_{yyy} + c_{zzz}) = 0 \tag{17}$$

The coefficients in Eq. (16) are so constructed that, along with Eq. (17), they ensure (and are equivalent to) the integral form of the divergence-free constraint:

$$\left(B_0^{x+} - B_0^{x-}\right) + \left(B_0^{y+} - B_0^{y-}\right) + \left(B_0^{z+} - B_0^{z-}\right) = 0 \tag{18}$$

This completes our description of the divergence-free reconstruction on the unit cube.

In practical situations, one might want to carry out the same procedure on a zone of size Δx, Δy and Δz in the x-, y- and z-directions, respectively. Notice that Eq. (18) then becomes:

$$\frac{1}{\Delta x}\left(B_0^{x+} - B_0^{x-}\right) + \frac{1}{\Delta y}\left(B_0^{y+} - B_0^{y-}\right) + \frac{1}{\Delta z}\left(B_0^{z+} - B_0^{z-}\right) = 0 \tag{19}$$

The problem can be mapped to a unit cube by dividing all the coefficients in Eqs. (4)–(6) by Δx, Δy and Δz, respectively. The method described in this section can now be applied to get the coefficients in Eqs. (7)–(9) and all the coefficients in those equations can subsequently be multiplied by Δx, Δy and Δz, respectively. This completes our description of the divergence-free reconstruction on any rectilinear mesh.

We make a few observations below:

(1) We observe that the normal components of the magnetic field in Eqs. (4)–(6) are indeed fourth order accurate in the faces. Furthermore, specifying all the moments in Eqs. (4)–(6) at the zone faces uniquely specifies all the coefficients in Eqs. (7)–(9) for the interior of that zone. Eqs. (7)–(9) contain all the terms that one would need in a fourth order accurate polynomial expansion for divergence-free functions. Thus all the fourth order accurate terms that are needed for reconstructing a divergence-free vector field in the interior of a zone are already provided by their fourth order accurate specification at the boundaries. The few remaining terms in Eqs. (7)–(9) only help in matching the magnetic fields exactly to the components at the boundaries. By dropping suitable terms in Eqs. (4)–(9) we can also see that all the third order accurate terms that are needed for reconstructing a divergence-free vector field in the interior of a zone are already provided by their third order accurate specification at the boundaries. A similar statement applies to the second order accurate reconstruction.

(2) Notice too that when carrying out adaptive mesh refinement of a divergence-free vector field by a refinement ratio of three, we need to specify 9 degrees of freedom at each boundary. This is because a coarse mesh face could overlie nine refined mesh faces, at which nine field components have been specified. The fourth order reconstruction presented here has 10 degrees of freedom at each boundary, see Eqs. (4)–(6). One degree of freedom can be relinquished either by setting $B^{x\pm}_{yyy} = B^{x\pm}_{zzz}$ or by setting $B^{x\pm}_{yyz} = B^{x\pm}_{yzz}$. Thus the reconstruction has sufficient amount of freedom to make it useful for carrying out adaptive mesh refinement with refinement ratios of three.
(3) Balsara [3] provided formulae for carrying out adaptive mesh refinement of a divergence-free vector field by a refinement ratio of two. The above point shows that a refinement ratio of three is also easy to achieve. Recursive application of the algorithms makes it possible to achieve refinement ratios that are any multiples or two and three. The algorithm presented here is dimensionally unsplit and offers analytic, closed form expressions for the reconstruction.
(4) Our formulation also minimizes the zone-averaged energy of the magnetic field. Since the pressure variable is derived from the total energy density, the minimization of the zone-averaged magnetic energy helps keep the pressure positive especially in problems with a very low plasma-β. We will later see in Section 5 that it helps keep the pressure positive when simulating the stringent test problem of a strong blast wave propagating through a very low-β plasma.
(5) The same transformations that were described in [4] for treating logically rectangular meshes with diagonal metrics go over transparently for the reconstruction given here. As a result, there are no obstacles to using the present formulation for designing MHD algorithms in cylindrical and spherical meshes. Similarly, one can use the present formulation for carrying out adaptive mesh refinement on such curvilinear meshes.
(6) The present formulation should also help in making divergence-free prolongation which is very useful in the construction of divergence-free multigrid schemes for resistive or Hall MHD.

3. Step-by-step description of the RK-WENO schemes for divergence-free MHD

The equations of ideal MHD can be cast in a conservative form that is suited for the design of higher order Godunov schemes. In that form they become:

$$\frac{\partial \mathbf{U}}{\partial t} + \frac{\partial \mathbf{F}}{\partial x} + \frac{\partial \mathbf{G}}{\partial y} + \frac{\partial \mathbf{H}}{\partial z} = 0 \tag{20}$$

where **F**, **G** and **H** are the ideal fluxes. Written out explicitly, Eq. (20) becomes:

$$\frac{\partial}{\partial t}\begin{pmatrix} \rho \\ \rho v_x \\ \rho v_y \\ \rho v_z \\ \varepsilon \\ B_x \\ B_y \\ B_z \end{pmatrix} + \frac{\partial}{\partial x}\begin{pmatrix} \rho v_x \\ \rho v_x^2 + P + \mathbf{B}^2/8\pi - B_x^2/4\pi \\ \rho v_x v_y - B_x B_y/4\pi \\ \rho v_x v_z - B_x B_z/4\pi \\ (\varepsilon + P + \mathbf{B}^2/8\pi) v_x - B_x(\mathbf{v}\cdot\mathbf{B})/4\pi \\ 0 \\ (v_x B_y - v_y B_x) \\ -(v_z B_x - v_x B_z) \end{pmatrix} + \frac{\partial}{\partial y}\begin{pmatrix} \rho v_y \\ \rho v_x v_y - B_x B_y/4\pi \\ \rho v_y^2 + P + \mathbf{B}^2/8\pi - B_y^2/4\pi \\ \rho v_y v_z - B_y B_z/4\pi \\ (\varepsilon + P + \mathbf{B}^2/8\pi) v_y - B_y(\mathbf{v}\cdot\mathbf{B})/4\pi \\ -(v_x B_y - v_y B_x) \\ 0 \\ (v_y B_z - v_z B_y) \end{pmatrix}$$
$$+ \frac{\partial}{\partial z}\begin{pmatrix} \rho v_z \\ \rho v_x v_z - B_x B_z/4\pi \\ \rho v_y v_z - B_y B_z/4\pi \\ \rho v_z^2 + P + \mathbf{B}^2/8\pi - B_z^2/4\pi \\ (\varepsilon + P + \mathbf{B}^2/8\pi) v_z - B_z(\mathbf{v}\cdot\mathbf{B})/4\pi \\ (v_z B_x - v_x B_z) \\ -(v_y B_z - v_z B_y) \\ 0 \end{pmatrix} = 0 \tag{21}$$

where ρ is the density, v_x, v_y and v_z are the velocity components, B_x, B_y and B_z are the magnetic field components, γ is the adiabatic index and $\varepsilon = \rho v^2/2 + P/(\gamma - 1) + \mathbf{B}^2/8\pi$ is the total energy. The equations for the density, momentum density and energy density parallel those in the Euler equations and can be discretized using standard WENO reconstruction in space along with Runge–Kutta formulations in time. While the magnetic fields seem to have a conservation law structure, an examination of the flux vectors show that the equations of MHD obey the following symmetries:

$$F_7 = -G_6, \quad F_8 = -H_6, \quad G_8 = -H_7 \tag{22}$$

These symmetries are also obeyed when any manner of non-ideal terms are introduced and are a fundamental consequence of the induction equation, see Eq. (1). Balsara and Spicer [10] realized how to use this dualism between the flux components and the electric fields to build electric fields at zone edges using the properly upwinded Godunov fluxes. Balsara [4] introduced a better way of obtaining the electric fields at zone edges that avoids spatial averaging. The Balsara and Spicer

[10] scheme is inherently second order accurate because of the spatial averaging. By overcoming this limitation, the scheme in [4] is easily extended to all orders. Once the electric fields are obtained at requisite collocation points on the zone edges a discrete version of Eq. (1) can be built, as shown in that paper. In that paper we also showed that Runge–Kutta time-discretizations could be used for MHD. We therefore describe the steps in the implementation of a Runge–Kutta time-discretiztion for MHD. The spatial representation is provided by an efficient implementation of a WENO scheme for structured meshes. A step-by-step description of the WENO scheme with Runge–Kutta time-stepping is provided below.

3.1. Divergence-free WENO reconstruction step

The first step in any finite volume scheme consists of obtaining a reconstruction of the field variables within a zone. Inclusion of the appropriate moments of the flow yields a correspondingly high accuracy. Thus at any stage in a multi-stage RK time-stepping scheme our first task is to obtain a representation of the flow in the following basis space:

$$\begin{aligned}\mathbf{U}(x,y,z) = {} & \overline{\mathbf{U}}_1 P_0(x)P_0(y)P_0(z) \\ & + \widehat{\mathbf{U}}_2 P_1(x)P_0(y)P_0(z) + \widehat{\mathbf{U}}_3 P_0(x)P_1(y)P_0(z) + \widehat{\mathbf{U}}_4 P_0(x)P_0(y)P_1(z) \qquad \leftarrow \text{ second order} \\ & + \widehat{\mathbf{U}}_5 P_2(x)P_0(y)P_0(z) + \widehat{\mathbf{U}}_6 P_0(x)P_2(y)P_0(z) + \widehat{\mathbf{U}}_7 P_0(x)P_0(y)P_2(z) \\ & + \widehat{\mathbf{U}}_8 P_1(x)P_1(y)P_0(z) + \widehat{\mathbf{U}}_9 P_0(x)P_1(y)P_1(z) + \widehat{\mathbf{U}}_{10} P_1(x)P_0(y)P_1(z) \qquad \leftarrow \text{ third order} \\ & + \widehat{\mathbf{U}}_{11} P_3(x)P_0(y)P_0(z) + \widehat{\mathbf{U}}_{12} P_0(x)P_3(y)P_0(z) + \widehat{\mathbf{U}}_{13} P_0(x)P_0(y)P_3(z) \\ & + \widehat{\mathbf{U}}_{14} P_2(x)P_1(y)P_0(z) + \widehat{\mathbf{U}}_{15} P_2(x)P_0(y)P_1(z) + \widehat{\mathbf{U}}_{16} P_1(x)P_2(y)P_0(z) + \widehat{\mathbf{U}}_{17} P_0(x)P_2(y)P_1(z) \\ & + \widehat{\mathbf{U}}_{18} P_1(x)P_0(y)P_2(z) + \widehat{\mathbf{U}}_{19} P_0(x)P_1(y)P_2(z) + \widehat{\mathbf{U}}_{20} P_1(x)P_1(y)P_1(z) \qquad \leftarrow \text{ fourth order}\end{aligned} \tag{23}$$

Here (x,y,z) denotes the local coordinates in the unit cube $[-1/2,1/2]\times[-1/2,1/2]\times[-1/2,1/2]$ to which the zone of interest is mapped and $\mathbf{U}(x,y,z)$ is the vector of conserved variables from Eq. (20). $\widehat{\mathbf{U}}_{2,\ldots,20}$ are the modes that are reconstructed at each time level for a fourth order scheme, with fewer modes needed for lower order schemes. The first five components of $\overline{\mathbf{U}}_1$ are just the zone-averaged mass, momentum and total energy densities that are available in each zone. The last three components of $\overline{\mathbf{U}}_1$ and $\widehat{\mathbf{U}}_{2,\ldots,20}$ have to be obtained from the divergence-free reconstruction of the magnetic field, whose facially averaged components are available at the appropriate faces. Using WENO reconstruction in each of the faces we obtain all the moments of Eqs. (4)–(6). The results of Section 2 then gives us all the moments of Eqs. (7)–(9) which also gives us the last three components of $\overline{\mathbf{U}}_1$ and $\widehat{\mathbf{U}}_{2,\ldots,20}$. WENO reconstruction can now be applied to obtain all the remaining components of $\widehat{\mathbf{U}}_{2,\ldots,20}$. Several good choices are available for WENO interpolation these days including the works of Jiang and Shu [29], Balsara and Shu [8], Dumbser and Käser [23] and Balsara et al. [5,7]. In [7] we presented a WENO reconstruction strategy that is very well-suited for structured meshes and we used that strategy here.

3.2. Flux and electric field evaluation step

A higher order scheme should also evaluate fluxes and electric fields with suitably high accuracy. Traditionally this has been done by solving a large number of Riemann problems at a large number of quadrature points, as was done in Cockburn and Shu [14]. A substantially simpler strategy was presented in Dumbser et al. [22] where the flux is viewed as a linear combination of four vectors. The four vectors are: (a) the conserved variables to the left of the zone boundary given by $\mathbf{U}_{L;i+1/2,j,k}(y,z)$, (b) the conserved variables to the right of the zone boundary given by $\mathbf{U}_{R;i+1/2,j,k}(y,z)$, (c) the flux to the left of the zone boundary given by $\mathbf{F}_{L;i+1/2,j,k}(y,z)$ and (d) the flux to the right of the zone boundary given by $\mathbf{F}_{R;i+1/2,j,k}(y,z)$. The strategy proposed by Dumbser et al. [22] applies to the space–time domain. We specialize it for the case where the time-averaging is not needed. Below it is instantiated for the linearized Riemann solver at any general point (y,z) on the x-boundary "$i+1/2,j,k$". Such a flux is described by:

$$\mathbf{F}_{i+1/2,j,k}(y,z) = \frac{1}{2}\left(\mathbf{F}_{L;i+1/2,j,k}(y,z) + \mathbf{F}_{R;i+1/2,j,k}(y,z)\right) - |A(y,z)|\left(\mathbf{U}_{R;i+1/2,j,k}(y,z) - \mathbf{U}_{L;i+1/2,j,k}(y,z)\right) \tag{24}$$

As written, the matrix $|A(y,z)|$ would have to be evaluated anew at each point (y,z) on the zone boundary. The essential insight from Dumbser et al. [22] consists of realizing that $|A(y,z)|$ can be evaluated once at the barycenter of the zone boundary. This is equivalent to freezing the dissipation model all over the zone boundary and it also makes the flux a linear function of the four vectors mentioned above. $\mathbf{U}_{L;i+1/2,j,k}(y,z)$ and $\mathbf{U}_{R;i+1/2,j,k}(y,z)$ are easily obtained once the reconstruction from Eq. (23) is available in the two zones that abut the zone face. In the companion ADER-WENO paper we present a very efficient strategy for obtaining $\mathbf{F}(x,y,z)$ within a zone when Eq. (23) is available in the zone. We also present explicit nodal locations within a control volume at which the vector of conserved variables, Eq. (23), needs to be evaluated. The fluxes in Eq. (21) are then evaluated at those nodes by using the vector of conserved variables. Once that is done, the companion ADER-WENO paper presents explicit formulae for obtaining a modal representation of the fluxes within each zone by using their nodal values. Appendix B, Section 3.2 and Appendix C from [7] present explicit formulae for second, third and fourth order schemes, respectively. Since a single stage of a Runge–Kutta scheme does not seek to make a space–time representation of the solution, one only needs to use the nodes that correspond to $\tau = 0$. Similarly, only those modes that are free of time-evo-

lution are needed. Appendix B of this paper shows how the third order ADER-WENO scheme described in Section 3.2 of [7] can be transcribed to form the much-simplified formulae needed for a third order WENO scheme with Runge–Kutta time-stepping. As a result, $\mathbf{F}_{L;i+1/2,j,k}(y,z)$ and $\mathbf{F}_{R;i+1/2,j,k}(y,z)$ are also easily obtained. With the frozen dissipation matrix, the right hand side of Eq. (24) is a linear combination of modal basis functions. Averaging Eq. (24) over the (y,z) coordinates of an x-face of the reference element only entails evaluating the integral analytically once and is easily done by using a symbolic manipulation package. A similar strategy can be applied at the y and z-faces.

The time-update can now be explicited for any stage in a multi-stage Runge–Kutta method. For instance, picking the second stage from Eq. (28) of the next section we obtain the equation that enables us to update the zone-centered conserved variables from a time t^n to a time $t^{n+1} = t^n + \Delta t$. It is given by

$$\overline{U}^{n+1}_{i,j,k} = \overline{U}^{n}_{i,j,k} - \frac{\Delta t}{\Delta x}(\overline{F}_{i+1/2,j,k} - \overline{F}_{i-1/2,j,k}) - \frac{\Delta t}{\Delta y}(\overline{G}_{i,j+1/2,k} - \overline{G}_{i,j-1/2,k}) - \frac{\Delta t}{\Delta z}(\overline{H}_{i,j,k+1/2} - \overline{H}_{i,j,k-1/2}) \tag{25}$$

Yee [40] showed that the divergence-free evolution of the field requires that a face-centered representation of the magnetic field be updated using an edge-centered representation of the electric field. Balsara and Spicer [10] showed that specific components of the flux vectors in Eq. (21) are indeed the components of the electric field from Eq. (2). They showed that the upwinded flux function can then be used to obtain the requisite properly upwinded components of the electric field. To instantiate the magnetic field update, we need to pick a specific stage in a multi-stage Runge–Kutta scheme. Let us do this for the second stage in Eq. (27). The magnetic field components are then updated from a time t^n to a time $t^{n+1} = t^n + \Delta t$ by the following update equations

$$\begin{aligned}
\overline{B}^{n+1}_{x;i+1/2,j,k} &= \overline{B}^{n}_{x;i+1/2,j,k} - \frac{\Delta t}{\Delta y \Delta z}(\Delta z \overline{E}_{z;i+1/2,j+1/2,k} - \Delta z \overline{E}_{z;i+1/2,j-1/2,k} + \Delta y \overline{E}_{y;i+1/2,j,k-1/2} - \Delta y \overline{E}_{y;i+1/2,j,k+1/2}) \\
\overline{B}^{n+1}_{y;i,j-1/2,k} &= \overline{B}^{n}_{y;i,j-1/2,k} - \frac{\Delta t}{\Delta x \Delta z}(\Delta x \overline{E}_{x;i,j-1/2,k+1/2} - \Delta x \overline{E}_{x;i,j-1/2,k-1/2} + \Delta z \overline{E}_{z;i-1/2,j-1/2,k} - \Delta z \overline{E}_{z;i+1/2,j-1/2,k}) \\
\overline{B}^{n+1}_{z;i,j,k+1/2} &= \overline{B}^{n}_{z;i,j,k+1/2} - \frac{\Delta t}{\Delta x \Delta y}(\Delta x \overline{E}_{x;i,j-1/2,k+1/2} - \Delta x \overline{E}_{x;i,j+1/2,k+1/2} + \Delta y \overline{E}_{y;i+1/2,j,k+1/2} - \Delta y \overline{E}_{y;i-1/2,j,k+1/2})
\end{aligned} \tag{26}$$

The electric fields in Eq. (26) are also easily obtained by averaging Eq. (24) suitably over the edges of the reference element and picking out the appropriate components of the fluxes. As in Dumbser et al. [22], we freeze the dissipation matrix at the barycenter of each edge, which makes the right hand side of Eq. (24) a linear combination of modal basis functions. Four electric field contributions are available at each edge, one from each of the four faces that come together at that edge. These four electric fields along each edge are averaged arithmetically, as in [4], to obtain the final electric field at the edge of interest. Balsara and Spicer [10] realized that the correct amount of upwinding for the electric fields in Eq. (26) could be a delicate issue, a topic that has also been addressed by Londrillo and DelZanna [32] and Gardiner and Stone [26]. Stable magnetic field evolution is achieved by drawing on those advances. This completes our description of the electric field evaluation for a specific stage in our multi-stage RK time-update. Similar update equations can be written for each and every stage of the RK time-updates detailed in the next subsection.

3.3. Multi-stage Runge–Kutta time-update step

The strong stability preserving Runge–Kutta schemes from Shu and Osher [37,38] are used for carrying out a time-update. At each stage of the multi-stage RK update, we apply the steps from Sections 3.1 and 3.2 to obtain the fluxes at each face and the electric field components at each edge. The Runge–Kutta time-stepping schemes consist of writing Eq. (1) for the magnetic field evolution and Eq. (20) for the evolution of the mass, momentum and energy densities in the form

$$\frac{d\mathbf{U}}{dt} = L(\mathbf{U}) \tag{27}$$

where $L(\mathbf{U})$ is a discretization of the spatial operator. The second order TVD Runge–Kutta scheme is simply the Heun scheme:

$$\begin{aligned}
\mathbf{U}^{(1)} &= \mathbf{U}^n + \frac{1}{2}\Delta t L(\mathbf{U}^n) \\
\mathbf{U}^{n+1} &= \mathbf{U}^n + \Delta t L(\mathbf{U}^{(1)})
\end{aligned} \tag{28}$$

The third order TVD Runge–Kutta scheme is given by:

$$\begin{aligned}
\mathbf{U}^{(1)} &= \mathbf{U}^n + \Delta t L(\mathbf{U}^n) \\
\mathbf{U}^{(2)} &= \frac{3}{4}\mathbf{U}^n + \frac{1}{4}\mathbf{U}^{(1)} + \frac{1}{4}\Delta t L(\mathbf{U}^{(1)}) \\
\mathbf{U}^{n+1} &= \frac{1}{3}\mathbf{U}^n + \frac{2}{3}\mathbf{U}^{(2)} + \frac{2}{3}\Delta t L(\mathbf{U}^{(2)})
\end{aligned} \tag{29}$$

The fourth order RK scheme from Shu and Osher [37] is rather complicated to implement and was not implemented here. As a result, the temporal update of the spatially fourth order scheme was always done with Eq. (29). For most applications

this yields a serviceable scheme that functions at a robust Courant number. However, when demonstrating the order of accuracy at fourth order in Section 4 we had to reduce the Courant number by a factor of ~0.396 for every doubling of the number of zones. This had to be done so that the third order temporal accuracy from Eq. (29) keeps step with the fourth order spatial accuracy. This deficiency is ameliorated by the ADER (for Arbitrary Derivative Riemann Problem) schemes presented in [7].

4. Accuracy analysis

The schemes presented here handily meet their design accuracies in one dimension. It is therefore interesting to present multi-dimensional tests showing high order of accuracy. Here we present a couple of demonstrations of high accuracy in two and three dimensions. A more extensive accuracy analysis for hydrodynamic and MHD problems has been catalogued in the companion paper on ADER-WENO schemes.

A couple of points need to be made about the simulations presented here. First, we used the slopes from the $r = 3$ WENO reconstruction of Jiang and Shu [29] for our second order scheme. As a result, the slopes have one more order of accuracy than the accuracy that would be furnished by a TVD-preserving limiter. This yields a very superior second order scheme. Second, for all the accuracy analyses presented in this section involving the spatially fourth order scheme, the Courant number was always decreased by a factor of 0.396 for every doubling of the number of zones.

4.1. Magnetized isodensity vortex in two dimensions

This test problem as described in [4] consists of a magnetized vortex moving across a domain given by $[-5,5]\times[-5,5]$ at an angle of 45° for a time of 10 units. For the fourth order scheme the domain is increased to $[-10,10]\times[-10,10]$ and the simulation time is increased to 20 units. This is done because the magnetic field has a Gaussian taper with increasing radius and the smaller domain retains a small but significant amount of magnetic field at the boundary. Had we used the smaller domain for the fourth order scheme, this small but spurious magnetic field would actually have been picked up by the scheme and its order property would have been damaged. The problem is initialized with an unperturbed flow of $(\rho,P,v_x,v_y,B_x,B_y)=(1,1,1,1,0,0)$. All boundaries are periodic. The ratio of the specific heat is set to $\gamma = 5/3$. The vortex is set up as a fluctuation of the unperturbed flow in the velocities and the magnetic field given by:

$$(\delta v_x,\delta v_y)=\frac{\kappa}{2\pi}e^{0.5(1-r^2)}(-y,x)$$
$$(\delta B_x,\delta B_y)=\frac{\mu}{2\pi}e^{0.5(1-r^2)}(-y,x)$$

The pressure fluctuation can be written as

$$\delta P=\frac{1}{8\pi}\left(\frac{\mu}{2\pi}\right)^2(1-r^2)e^{(1-r^2)}-\frac{1}{2}\left(\frac{\kappa}{2\pi}\right)^2e^{(1-r^2)}$$

The density is set to unity. A Courant number of 0.4 was used for all the second and third order test problems and also for the coarsest mesh in the fourth order test problem. A linearized Riemann solver from Balsara [1] was used.

Table 1 shows the results of the accuracy analysis. The error is measured in the x-component of the magnetic field. All the schemes meet their design accuracies. Notice that the third order scheme at 128×128 zone resolution shows the same L_1 error as the second order scheme at 256×256 zone resolution. We see therefore that higher order schemes deliver a much improved solution quality compared to lower order schemes on meshes of the same resolution. Furthermore, the higher order schemes need far fewer zones to achieve the same accuracy as a lower order scheme. Table 1 therefore illustrates the utility of higher order schemes very nicely.

Table 1
The accuracy analysis for the two-dimensional isodensity vortex problem is tabulated here using the second, third and fourth order schemes presented in this paper. The error is measured in the x-component of the magnetic field.

Method	Number of zones	L_1 error	L_1 order	L_∞ error	L_∞ order
Second order RK-WENO	32×32	1.15689×10^{-2}		0.189318	
	64×64	3.74953×10^{-3}	1.62	6.00319×10^{-2}	1.66
	128×128	9.57467×10^{-4}	1.97	1.53503×10^{-2}	1.97
	256×256	2.39584×10^{-4}	2.00	3.83531×10^{-3}	2.00
Third order RK-WENO	32×32	5.53837×10^{-3}		9.79331×10^{-2}	
	64×64	9.77841×10^{-4}	2.50	1.75191×10^{-2}	2.48
	128×128	1.27506×10^{-4}	2.94	2.36221×10^{-3}	2.89
	256×256	1.60549×10^{-5}	2.99	2.99136×10^{-4}	2.98
Fourth order RK-WENO	32×32	2.96778×10^{-3}		0.103623	
	64×64	1.56211×10^{-4}	4.25	5.21875×10^{-3}	4.31
	128×128	7.33125×10^{-6}	4.41	2.45447×10^{-4}	4.41

Table 2
The accuracy analysis for the three-dimensional torsional Alfven wave problem is presented here using the second, third and fourth order schemes. The errors are measured in the x-component of the magnetic field.

Method	Number of zones	L_1 error	L_1 order	L_∞ error	L_∞ order
Second order RK-WENO	$8\times8\times8$	3.46827×10^{-2}		5.17569×10^{-2}	
	$16\times16\times16$	2.25885×10^{-2}	0.62	3.57951×10^{-2}	0.53
	$32\times32\times32$	4.87419×10^{-3}	2.21	7.68322×10^{-3}	2.22
	$48\times48\times48$	1.77966×10^{-3}	2.48	2.79747×10^{-3}	2.49
Third order RK-WENO	$8\times8\times8$	3.56043×10^{-2}		5.32694×10^{-2}	
	$16\times16\times16$	1.65967×10^{-2}	1.10	2.56119×10^{-2}	1.06
	$32\times32\times32$	2.65506×10^{-3}	2.64	4.17435×10^{-3}	2.62
	$48\times48\times48$	8.05482×10^{-4}	2.94	1.27225×10^{-3}	2.93
Fourth order RK-WENO	$8\times8\times8$	2.52284×10^{-2}		3.82295×10^{-2}	
	$16\times16\times16$	1.17975×10^{-3}	4.42	1.85115×10^{-3}	4.37
	$32\times32\times32$	5.29206×10^{-5}	4.48	8.38025×10^{-5}	4.47

4.2. Torsional Alfven wave propagation in three dimensions

The previous test problem used a flow that was an exact, equilibrium structure of the governing equations. Although torsional Alfven waves also satisfy the governing equations, they are susceptible to parametric instabilities. These instabilities exist at low values of plasma-β, see Goldstein [27] and Del Zanna et al. [19], and also at high values of plasma-β, see Jayanti and Hollweg [28]. The present test problem is designed to ameliorate such instabilities as far as possible.

In this problem we initialize a torsional Alfven wave along the x' axis of an (x',y',z') coordinate system with the following parameters

$$\rho = 1, \quad P = 1000, \quad \Phi = \frac{2\pi}{\lambda}(x' - 2t)$$
$$v_{x'} = 1, \quad v_{y'} = \varepsilon\cos\Phi, \quad v_{z'} = \varepsilon\sin\Phi$$
$$B_{x'} = \sqrt{4\pi\rho}, \quad B_{y'} = -\varepsilon\sqrt{4\pi\rho}\cos\Phi, \quad B_{z'} = -\varepsilon\sqrt{4\pi\rho}\sin\Phi$$

Here we take $\varepsilon = 0.02$ and $\lambda = \sqrt{3}$. The magnetic vector potential is also useful when initializing a divergence-free magnetic field on a mesh and is given by

$$A_{x'} = 0, \quad A_{y'} = \varepsilon\lambda\sqrt{\rho/\pi}\cos\Phi, \quad A_{z'} = \sqrt{4\pi\rho}y' + \varepsilon\lambda\sqrt{\rho/\pi}\sin\Phi$$

The actual problem is solved on a unit cube in the (x,y,z) coordinate frame which is rotated relative to the (x',y',z') coordinate system. The rotation matrix is called **A** and is given by

$$\mathbf{A} = \begin{bmatrix} \cos\psi\cos\phi - \cos\theta\sin\phi\sin\psi & \cos\psi\sin\phi + \cos\theta\cos\phi\sin\psi & \sin\psi\sin\theta \\ -\sin\psi\cos\phi - \cos\theta\sin\phi\cos\psi & -\sin\psi\sin\phi + \cos\theta\cos\phi\cos\psi & \cos\psi\sin\theta \\ \sin\theta\sin\phi & -\sin\theta\cos\phi & \cos\theta \end{bmatrix}$$

where $\phi = -\pi/4$, $\theta = \sin^{-1}\left(-\sqrt{2/3}\right)$ and $\psi = \sin^{-1}\left(\left(\sqrt{2}-\sqrt{6}\right)/4\right)$. As a result, the position vector $\mathbf{r}'$ in the primed frame transforms to the position vector $\mathbf{r}$ in the unprimed frame as $\mathbf{r} = \mathbf{A}\mathbf{r}'$. Other vectors transform similarly. Other formulations of the rotation matrix are indeed possible, but the one in the above equation works very well. Application of the rotation matrix makes the wave propagate along the diagonal of the unit cube. The wave propagates at a speed of 2 units. The problem is stopped at a time of $\sqrt{3}/2$ by which time the wave has propagated once around the unit cube. A Courant number of 0.3 was used for all the second and third order test problems and also for the coarsest mesh in the fourth order test problem. A linearized Riemann solver was used.

Table 2 presents the accuracy analysis for schemes up to fourth order. Please recall that the combination of a spatially fourth order scheme with a temporally third order RK scheme required us to use a diminishing Courant number with increasing resolution at fourth order and only at fourth order. As a result, the accuracy analysis of the fourth order scheme had to be restricted to smaller meshes. In [7], we present schemes that overcome this limitation. Table 2 is nevertheless very illustrative. It shows that all the schemes presented here meet their design accuracies. We see that even on very coarse meshes, such as the $16\times16\times16$ mesh in Table 1, the fourth order scheme offers more than one order of magnitude improvement over the second order scheme. Table 2 therefore demonstrates the utility of higher order schemes.

5. Test problems

In this section we present several tests for the schemes that have been designed here. Because the divergence-free reconstruction of the magnetic field only comes to the fore in multiple dimensions, all of the tests presented here are inherently two-dimensional and were run with a Courant number of 0.4.

5.1. Numerical dissipation and long-term decay of alfven waves in two dimensions

This test problem was first presented in [4] and examines the dissipation of torsional Alfven waves in two dimensions. Other practitioners, Ryu et al. [36], Balsara and Spicer [10] and Toth [39], have also see the utility of Alfven wave decay in revealing the numerical dissipation of MHD schemes. Here the torsional Alfven waves propagate at an angle of $\tan^{-1}(1/r) = \tan^{-1}(1/6) = 9.462^\circ$ to the y-axis through a domain given by $[-r/2, r/2] \times [-r/2, r/2]$ with $r = 6$. The problem was initialized on a computational domain with 120×120 zones. Periodic boundary conditions were enforced. The pressure and density are uniformly initialized as $P_0 = 1$ and $\rho_0 = 1$. The unperturbed velocity and unperturbed magnetic field are given by $v_0 = 0$ and $B_0 = 1$. The amplitude of the Alfven waves is parametrized by ε, which is set to 0.2. The simulation was stopped at 129 time units by which time the waves had crossed the domain several times. The CFL number was set to 0.4 for all the schemes presented here. The direction of the wave propagation along the unit vector can be written as

$$\hat{n} = n_x\hat{i} + n_y\hat{j} = \frac{1}{\sqrt{r^2+1}}\hat{i} + \frac{r}{\sqrt{r^2+1}}\hat{j}$$

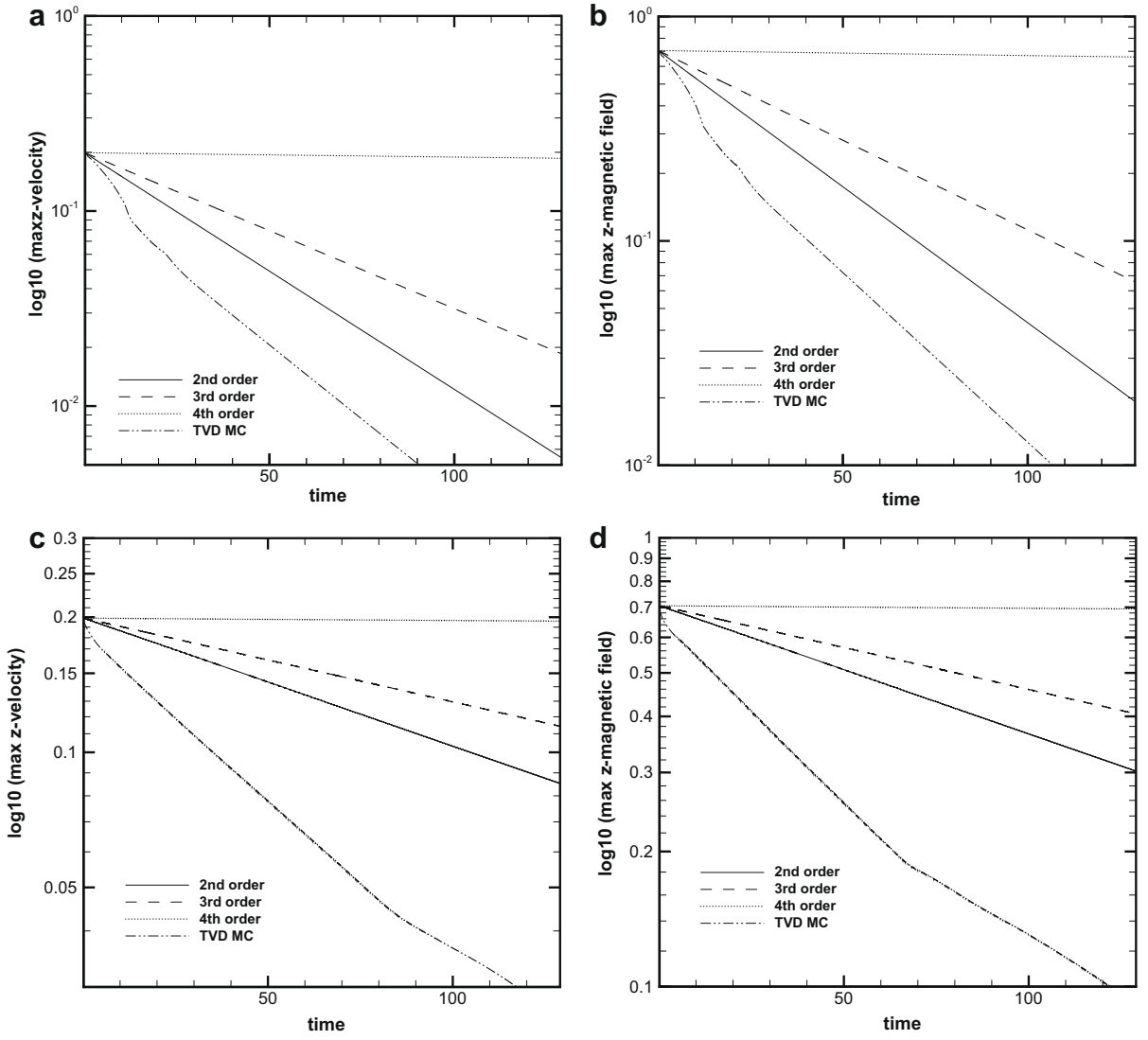

Fig. 1. The log-linear plots show the decay of torsional Alfven waves that propagate obliquely on a two-dimensional square. The top two panels show the decay of the maximum z-velocity and the maximum z-component of the magnetic field when second, third and fourth order schemes are used with an HLLE Riemann solver. The bottom two panels show the same information when a linearized Riemann solver is used. For comparison purposes, the results from a TVD scheme with MC limiter are also shown. Temporally third order RK updates were used for the spatially fourth order scheme. Observe that the decay is substantially reduced with increasing spatial order. Also observe that the linearized Riemann solver provides a substantial improvement to the solution, especially at lower orders.

The phase of the waves is given by

$$\phi = \frac{2\pi}{n_y}(n_x x + n_y y - V_A t), \quad \text{where } V_A = \frac{B_0}{\sqrt{4\pi\rho_0}}$$

The velocity is given by

$$\mathbf{v} = (v_0 n_x - \varepsilon n_y \cos\phi)\hat{i} + (v_0 n_y + \varepsilon n_x \cos\phi)\hat{j} + \varepsilon \sin\phi \hat{k}$$

The magnetic field is given by

$$\mathbf{B} = \left(B_0 n_x + \varepsilon n_y \sqrt{4\pi\rho_0}\cos\phi\right)\hat{i} + \left(B_0 n_y - \varepsilon n_x \sqrt{4\pi\rho_0}\cos\phi\right)\hat{j} - \varepsilon\sqrt{4\pi\rho_0}\sin\phi\hat{k}$$

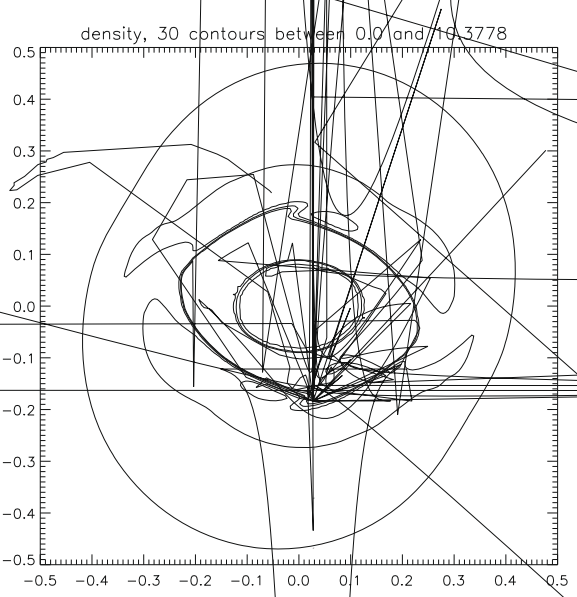

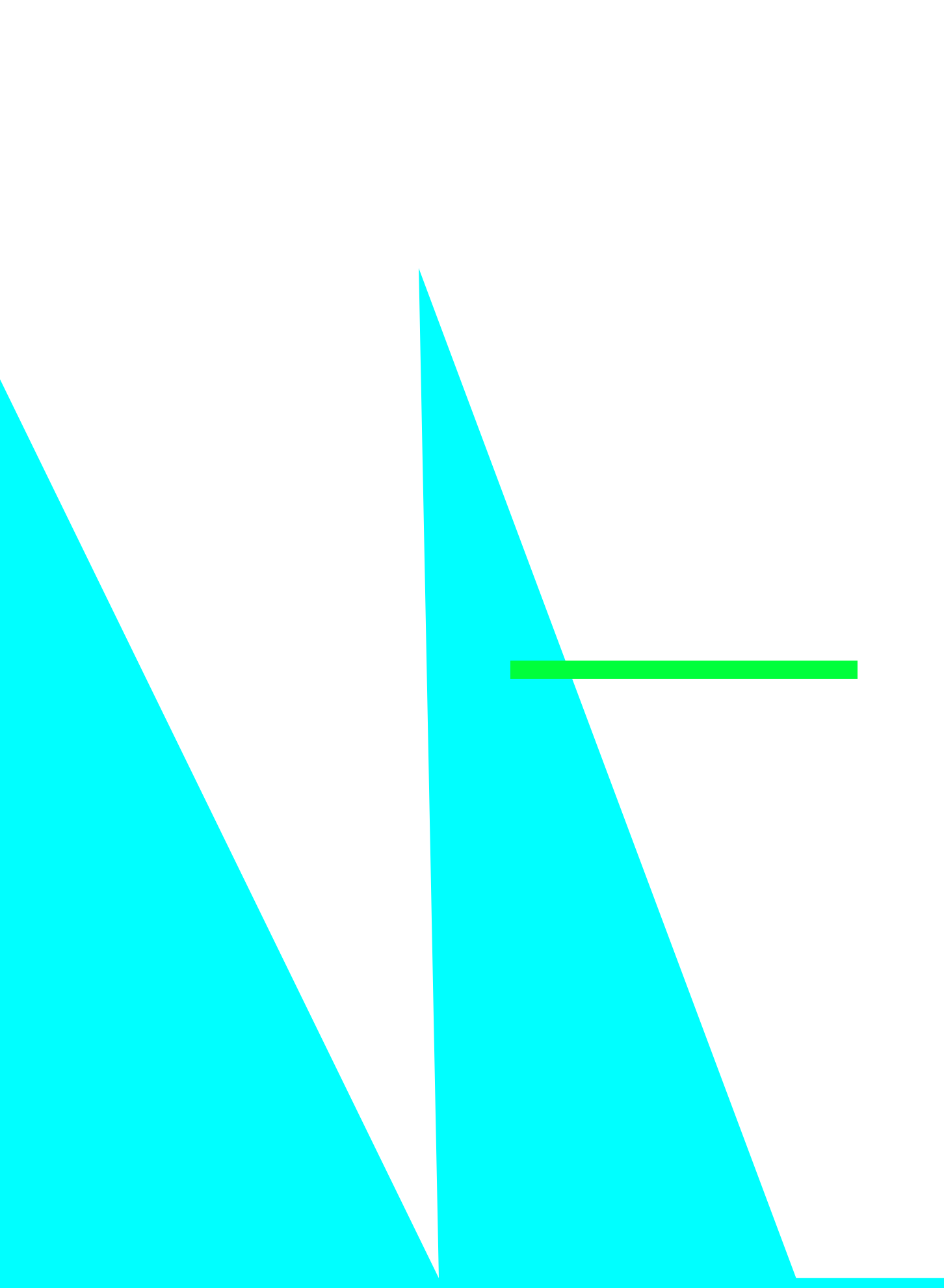

show the z-components of the velocity and magnetic field, the fluctuating part of all other vectorial entities would show a similar decay. As a result, it is not worthwhile to plot out the other components of the velocity or the magnetic field. We see that regardless of the Riemann solver used, increasing the order of accuracy provides a substantial reduction in the numerical dissipation. Thus higher order schemes are favored for the simulation of complex phenomena involving wave propagation. For the lower order schemes the linearized Riemann solver offers a significant improvement over the HLL Riemann solver. However, this advantage is diminished with increasing order. We therefore see that higher order schemes allow us to get by with less expensive Riemann solvers.

5.2. The rotor problem in two dimensions

The two-dimensional rotor problem was presented in Balsara and Spicer [10] and in Balsara [4]. The description in those papers is quite thorough. As a result the problem description is not repeated here. The problem was set up on a 200×200 zone mesh and was run with a Courant number of 0.4 to a completion time of 0.29 units. The spatially fourth order WENO scheme with a third order RK time-stepping strategy and a linearized Riemann solver were used. Fig. 2 shows the density, pressure, Mach number and the magnitude of the magnetic field. The results are very consistent with those from Balsara and Spicer [10] showing that the divergence-free reconstruction presented here performs well on multi-dimensional MHD problems.

5.3. The blast problem in two dimensions

This two-dimensional problem was first presented by Balsara and Spicer [10]. It has also been described in detail in [4] and we do not repeat the same description here. The fourth order WENO scheme with a third order RK time-stepping strategy and an HLL Riemann solver was applied to a mesh having 200×200 zones. The problem was run with a Courant number of 0.4 and was stopped at a time of 0.01 units. The problem results in an extremely strong, almost circular fast magnetosonic shock propagating at all possible angles to the magnetic field in the low-β ambient plasma. The plasma-β is 0.000251 making this a challenging test problem. Fig. 3 shows the logarithm (base 10) of the density, the logarithm of the pressure, the magnitude of the velocity and the magnitude of the magnetic field. We see that all structures are captured crisply. The positivity of the pressure is maintained even in regions where the strong shock propagates obliquely to the mesh. This shows that the divergence-free reconstruction strategies and the resultant high order schemes presented here perform well on stringent multi-dimensional MHD problems involving low-β plasmas.

6. Conclusions

The work presented here enables us to come to the following conclusions:

(1) Following a line of development begun in Balsara [3], we show that the problem of reconstructing divergence-free vector fields can be carried out to higher orders. This has been done for orders up to four. Close form expressions have been provided in Section 2 with several further details catalogued in Appendix A.
(2) Following a line of development begun in [4], we show that the above development yields divergence-free RK-WENO schemes with order of accuracy that is better than second. In particular, we explore the third and fourth order accurate schemes here. Some details for their efficient implementation have been provided in Appendix B. The reader is also invited to read [7] for even more details on implementation for all orders up to fourth.
(3) When applied to smooth test problems, the schemes have been shown to meet their design accuracies.
(4) Using a stringent set of test problems we show that the schemes presented here effectively combine the dual, and often-conflicting demands of capturing very strong shocks and retaining low dissipation in contact discontinuities and Alfven waves. This shows the effectiveness of our schemes for numerical MHD.

Acknowledgments

D.S.B. acknowledges support via NSF Grant AST-0607731. D.S.B. also acknowledges NASA Grants HST-AR-10934.01-A, NASA-NNX07AG93G and NASA-NNX08AG69G. The majority of simulations were performed on PC clusters at UND but a few initial simulations were also performed at NASA-NCCS.

Appendix A

When the divergence-free constraint is applied to the quartic terms in Eqs. (7)–(9) we get

$$a_{xxxx} = -\frac{1}{4}(b_{xxxy} + c_{xxxz}) \tag{A.1}$$

$$3a_{xxxy} + 2b_{xxyy} = -c_{xxyz} \tag{A.2}$$

$$3a_{xxxz} + 2c_{xxzz} = -b_{xxyz} \tag{A.3}$$

The full set of nine constraints at fourth order can be obtained by making all cyclic rotations of variables in Eqs. (A.1)–(A.3). We see that Eq. (A.1) directly gives us a_{xxxx} because its right hand side is known by the time we sequentially arrive at Eq. (11). However, notice that Eq. (A.2) does not enable us to uniquely specify a_{xxxy} and b_{xxyy}. Likewise, Eq. (A.3) does not offer a unique specification of a_{xxxz} and c_{xxzz}. To uniquely specify those terms we have to minimize the integral of the magnetic energy over the zone being considered. The orthogonality of the Legendre polynomials permits us to evaluate the integral analytically. The full integral has a large number of terms, so we only focus on the terms that are relevant to our narrative. Thus we have:

$$\iiint_V \mathbf{B}^2(x,y,z)dV = \cdots + \frac{1}{33,600}a_{xxxy}^2 + \frac{1}{32,400}b_{xxyy}^2 + \frac{1}{33,600}a_{xxxz}^2 + \frac{1}{32,400}c_{xxzz}^2 + \cdots \tag{A.4}$$

We express b_{xxyy} in terms of a_{xxxy} and c_{xxyz} using Eq. (A.2) and, furthermore, we express c_{xxzz} in terms of a_{xxxz} and b_{xxyz} with the help of Eq. (A.3). Then substituting b_{xxyy} and c_{xxzz} into Eq. (A.4) permits us to minimize the energy of the magnetic field while simultaneously yielding unique expressions for b_{xxyy}, a_{xxxy}, c_{xxzz} and a_{xxxz}. The final expressions have been given in Eq. (11) in a format that facilitates a cyclic rotation of variables.

When the divergence-free constraint is applied to the third order terms in Eqs. (7)–(9) we get

$$a_{xxx} = -\frac{1}{3}(b_{xxy} + c_{xxz}) \tag{A.5}$$

$$a_{xxy} + b_{xyy} = -c_{xyz}/2 \tag{A.6}$$

The full set of six constraints at third order can be obtained by making all cyclic rotations of variables in Eqs. (A.5) and (A.6). We see that Eq. (A.5) directly gives us a_{xxx} because its right hand side is known by the time we arrive at Eq. (13). To uniquely specify a_{xxy} and b_{xyy} we need to minimize the magnetic energy as before. The final expressions have been given in Eq. (13) in a format that facilitates a cyclic rotation of variables. This completes our description of the SVD minimization.

The equations that result when the divergence-free constraint is applied to the second and first order terms in Eqs. (7)–(9) are catalogued in Eqs. (15) and (17), respectively.

Appendix B

For a third order RK-WENO scheme we start with the modal representation of the conserved variables which is given by:

$$\begin{aligned} u(\xi,\eta,\zeta) = {} & \hat{w}_1 P_0(\xi)P_0(\eta)P_0(\zeta) \\ & + \hat{w}_2 P_1(\xi)P_0(\eta)P_0(\zeta) + \hat{w}_3 P_0(\xi)P_1(\eta)P_0(\zeta) + \hat{w}_4 P_0(\xi)P_0(\eta)P_1(\zeta) \\ & + \hat{w}_5 P_2(\xi)P_0(\eta)P_0(\zeta) + \hat{w}_6 P_0(\xi)P_2(\eta)P_0(\zeta) + \hat{w}_7 P_0(\xi)P_0(\eta)P_2(\zeta) \\ & + \hat{w}_8 P_1(\xi)P_1(\eta)P_0(\zeta) + \hat{w}_9 P_0(\xi)P_1(\eta)P_1(\zeta) + \hat{w}_{10} P_1(\xi)P_0(\eta)P_1(\zeta) \end{aligned}$$

The coordinates (ξ,η,ζ) span the reference element $[-1/2,1/2]\times[-1/2,1/2]\times[-1/2,1/2]$. Consequently, the variables in a physical zone can easily be mapped to this reference element. We then define the vector of conserved variables at the fifteen symmetrically-placed nodal points given by the ordered set

$$\begin{aligned} & \{(0,0,0);\ (1/2,0,0);\ (-1/2,0,0);\ (0,1/2,0);\ (0,-1/2,0);\ (0,0,1/2);\ (0,0,-1/2);\ (1/2,1/2,1/2); \\ & \quad (-1/2,1/2,1/2);\ (1/2,-1/2,1/2);\ (-1/2,-1/2,1/2);\ (1/2,1/2,-1/2);\ (-1/2,1/2,-1/2); \\ & \quad (1/2,-1/2,-1/2);\ (-1/2,-1/2,-1/2)\} \end{aligned}$$

Let $\{\bar{u}_1,\ldots,\bar{u}_{15}\}$ be the ordered set of conserved variables evaluated at these nodal points. Use these nodal values of the conserved variables to obtain the nodal values of all three flux vectors. We focus on the x-flux and write the corresponding ordered set of x-fluxes as $\{\bar{f}_1,\ldots,\bar{f}_{15}\}$. The modal form of the x-flux within the reference element can then be written as

$$\begin{aligned} f(\xi,\eta,\zeta) = {} & \hat{f}_1 P_0(\xi)P_0(\eta)P_0(\zeta) \\ & + \hat{f}_2 P_1(\xi)P_0(\eta)P_0(\zeta) + \hat{f}_3 P_0(\xi)P_1(\eta)P_0(\zeta) + \hat{f}_4 P_0(\xi)P_0(\eta)P_1(\zeta) \\ & + \hat{f}_5 P_2(\xi)P_0(\eta)P_0(\zeta) + \hat{f}_6 P_0(\xi)P_2(\eta)P_0(\zeta) + \hat{f}_7 P_0(\xi)P_0(\eta)P_2(\zeta) \\ & + \hat{f}_8 P_1(\xi)P_1(\eta)P_0(\zeta) + \hat{f}_9 P_0(\xi)P_1(\eta)P_1(\zeta) + \hat{f}_{10} P_1(\xi)P_0(\eta)P_1(\zeta) \end{aligned}$$

and its modal coefficients $\{\hat{f}_1,\ldots,\hat{f}_{10}\}$ are obtained by the transcription

$$\begin{aligned} \hat{f}_1 &= (\bar{f}_2 + \bar{f}_3 + \bar{f}_4 + \bar{f}_5 + \bar{f}_6 + \bar{f}_7)/6 \\ \hat{f}_2 &= \bar{f}_2 - \bar{f}_3 \\ \hat{f}_3 &= \bar{f}_4 - \bar{f}_5 \\ \hat{f}_4 &= \bar{f}_6 - \bar{f}_7 \\ \hat{f}_5 &= 2\bar{f}_2 - 4\bar{f}_1 + 2\bar{f}_3 \\ \hat{f}_6 &= 2\bar{f}_4 - 4\bar{f}_1 + 2\bar{f}_5 \end{aligned}$$

$$\hat{f}_7 = 2\bar{f}_6 - 4\bar{f}_1 + 2\bar{f}_7$$
$$\hat{f}_8 = (\bar{f}_8 - \bar{f}_9 - \bar{f}_{10} + \bar{f}_{11} + \bar{f}_{12} - \bar{f}_{13} - \bar{f}_{14} + \bar{f}_{15})/2$$
$$\hat{f}_9 = (\bar{f}_8 + \bar{f}_9 - \bar{f}_{10} - \bar{f}_{11} - \bar{f}_{12} - \bar{f}_{13} + \bar{f}_{14} + \bar{f}_{15})/2$$
$$\hat{f}_{10} = (\bar{f}_8 - \bar{f}_9 + \bar{f}_{10} - \bar{f}_{11} - \bar{f}_{12} + \bar{f}_{13} - \bar{f}_{14} + \bar{f}_{15})/2$$

Please observe that $u(\xi = +1/2, \eta, \zeta)$ and $f(\xi = +1/2, \eta, \zeta)$ can easily be used to obtain the conserved variables and the fluxes at the right face of the reference element. The modal representation now makes it very easy to obtain area averages over the right face, as is needed for the flux in Eq. (24). Areal averages for the left face are similarly obtained. Likewise, the line averages at the zone edges that are needed for the electric field evaluation are also easily obtained. These averages are best done by using a symbolic manipulation package.

The present appendix provides all the details that are needed for third order schemes. Appendices B and C from [7] provide analogous details for second and fourth order schemes, respectively.

References

[1] D.S. Balsara, Linearized formulation of the Riemann problem for adiabatic and isothermal magnetohydrodynamics, Astrophysical Journal Supplement 116 (1998) 119.
[2] D.S. Balsara, Total variation diminishing algorithm for adiabatic and isothermal magnetohydrodynamics, Astrophysical Journal Supplement 116 (1998) 133.
[3] D.S. Balsara, Divergence-free adaptive mesh refinement for magnetohydrodynamics, Journal of Computational Physics 174 (2001) 614–648.
[4] D.S. Balsara, Second-order-accurate schemes for magnetohydrodynamics with divergence-free reconstruction, Astrophysical Journal Supplement 151 (2004) 149–184.
[5] D.S. Balsara, C. Altmann, C.D. Munz, M. Dumbser, A sub-cell based indicator for troubled zones in RKDG schemes and a novel class oh hybrid RKDG + HWENO schemes, Journal of Computational Physics 226 (2007) 586–620.
[6] D.S. Balsara, J.S. Kim, An intercomparison between divergence-cleaning and staggered mesh formulations for numerical magnetohydrodynamics, Astrophysical Journal 602 (2004) 1079.
[7] D.S. Balsara, T. Rumpf, M. Dumbser, C.-D. Munz, Efficient, high accuracy ADER-WENO schemes for hydrodynamics and divergence-free magnetohydrodynamics, Journal of Computational Physics 228 (2009) 2480–2516.
[8] D.S. Balsara, C.-W. Shu, Monotonicity preserving weighted non-oscillatory schemes WIRH increasingly high order of accuracy, Journal of Computational Physics 160 (2000) 405–452.
[9] D.S. Balsara, D.S. Spicer, Maintaining pressure positivity in magnetohydrodynamic simulations, Journal of Computational Physics 148 (1999) 133–148.
[10] D.S. Balsara, D.S. Spicer, A staggered mesh algorithm using high order Godunov fluxes to ensure solenoidal magnetic fields in magnetohydrodynamic simulations, Journal of Computational Physics 149 (1999) 270–292.
[11] J.U. Brackbill, D.C. Barnes, The effect of nonzero $\nabla \cdot \mathbf{B}$ on the numerical solution of the magnetohydrodynamic equations, Journal of Computational Physics 35 (1980) 426–430.
[12] S.H. Brecht, J.G. Lyon, J.A. Fedder, K. Hain, A simulation study of east–west IMF effects on the magnetosphere, Geophysical Research Letters 8 (1981) 397.
[13] M. Brio, C.C. Wu, An upwind differencing scheme for the equations of ideal magnetohydrodynamics, Journal of Computational Physics 75 (1988) 400.
[14] B. Cockburn, C.-W. Shu, The Runge–Kutta discontinuous Galerkin method for Conservation Laws V, Journal of Computational Physics 141 (1998) 199–224.
[15] R.K. Crockett, P. Colella, R.T. Fisher, R.I. Klein, C.F. McKee, An unsplit cell-centered Godunov method for ideal MHD, Journal of Computational Physics 203 (2005) 422.
[16] W. Dai, P.R. Woodward, An approximate Riemann solver for ideal magnetohydrodynamics, Journal of Computational Physics 111 (1994) 354–372.
[17] W. Dai, P.R. Woodward, On the divergence-free condition and conservation laws in numerical simulations for supersonic magnetohydrodynamic flows, Astrophysical Journal 494 (1998) 317–335.
[18] A. Dedner, F. Kemm, D. Kröener, C.-D. Munz, T. Schnitzer, M. Wesenberg, Hyperbolic divergence cleaning for MHD equations, Journal of Computational Physics 175 (2002) 645–673.
[19] L. Del Zanna, M. Velli, P. Londrillo, Parametric decay of circularly polarized Alfvén waves: multidimensional simulations in periodic and open domains, Astronomy and Astrophysics 367 (2001) 705–718.
[20] C.R. DeVore, Flux-corrected transport techniques for multidimensional compressible magnetohydrodynamics, Journal of Computational Physics 92 (1991) 142–160.
[21] M. Dumbser, D. Balsara, E.F. Toro, C.D. Munz, A unified framework for the construction of one-step finite volume and discontinuous Galerkin schemes on unstructured meshes, Journal of Computational Physics 227 (2008) 8209–8253.
[22] M. Dumbser, M. Käser, V.A. Titarev, E.F. Toro, Quadrature-free non-oscillatory finite volume schemes on unstructured meshes for nonlinear hyperbolic systems, Journal of Computational Physics 226 (2007) 204–243.
[23] M. Dumbser, M. Käser, Arbitrary high order non-oscillatory finite volume schemes on unstructured meshes for linear hyperbolic systems, Journal of Computational Physics 221 (2007) 693–723.
[24] C.R. Evans, J.F. Hawley, Simulation of magnetohydrodynamic flows: a constrained transport method, Astrophysical Journal 332 (1989) 659.
[25] S.A.E.G. Falle, S.S. Komissarov, P. Joarder, A multidimensional upwind scheme for magnetohydrodynamics, Monthly Notices of the Royal Astronomical Society 297 (1998) 265–277.
[26] T. Gardiner, J.M. Stone, Journal of Computational Physics 295 (2005) 509.
[27] M.L. Goldstein, An instability of finite amplitude circularly polarized Alfven waves, Astrophysical Journal 219 (1978) 700.
[28] V. Jayanti, J.V. Hollweg, On the dispersion relations for parametric instabilities of parallel-propagating Alfvén waves, Journal of Geophysical Research 98 (1993) 13247–13252.
[29] G.-S. Jiang, C.-W. Shu, Efficient implementation of weighted ENO schemes, Journal of Computational Physics 126 (1996) 202–228.
[30] G.-S. Jiang, C.C. Wu, A high-order WENO finite difference scheme for the equations of ideal magnetohydrodynamics, Journal of Computational Physics 150 (2) (1999) 561–594.
[31] S. Li, High order central scheme on overlapping cells for magneto-hydrodynamic flows with and without constrained transport method, Journal of Computational Physics 227 (15) (2008) 7368–7393.
[32] P. Londrillo, L. DelZanna, On the divergence-free condition in Godunov-type schemes for ideal magnetohydrodynamics: the upwind constrained transport method, Journal of Computational Physics 195 (2004) 17–48.
[33] K.G. Powell, An Approximate Riemann Solver for MHD (that actually works in more than one dimension), ICASE Report No. 94-24, Langley, VA, 1994.
[34] P.L. Roe, D.S. Balsara, Notes on the eigensystem of magnetohydrodynamics, SIAM Journal of Applied Mathematics 56 (1996) 57.
[35] D. Ryu, T.W. Jones, Numerical MHD in astrophysics: algorithm and tests for one-dimensional flow, Astrophysical Journal 442 (1995) 228.

[36] D. Ryu, F. Miniati, T.W. Jones, A. Frank, A divergence-free upwind code for multidimensional magnetohydrodynamic flows, Astrophysical Journal 509 (1998) 244–255.
[37] C.-W. Shu, S.J. Osher, Efficient implementation of essentially non-oscillatory shock capturing schemes, Journal of Computational Physics 77 (1988) 439–471.
[38] C.-W. Shu, S.J. Osher, Efficient implementation of essentially non-oscillatory shock capturing schemes II, Journal of Computational Physics 83 (1989) 32–78.
[39] G. Toth, The $\nabla \cdot B = 0$ constraint in shock-capturing MHD codes, Journal of Computational Physics 161 (2000) 605.
[40] K.S. Yee, Numerical solution of initial boundary value problems involving maxwell equation in an isotropic media, IEEE Transactions on Antennas and Propagation 14 (1966) 302.
[41] A.L. Zachary, A. Malagoli, P. Colella, A higher-order Godunov method for multi-dimensional ideal magnetohydrodynamics, SIAM Journal of Scientific Computing 15 (1994) 263.